Polyhedron 262 (2024) 117161

Contents lists available at ScienceDirect

Polyhedron

journal homepage: www.elsevier.com/locate/poly

Synthesis and characterisation of dipyrromethene Cu(II) complexes: A preliminary DNA intercalation study

Nabeelah Sarang, Matthew L. Bracken *, Monika Nowakowska, Sadhna Mathura *

Molecular Sciences Institute, School of Chemistry, University of the Witwatersrand, PO Wits 2050, Johannesburg, South Africa

ARTICLE INFO

Keywords:
Dipyrromethene
Copper chelate
Crystal structure
DNA binding
Docking

ABSTRACT

Copper complexes of the bilirubin bile pigment have been shown to affect DNA. It was suggested that the copper ions within these metal-bilirubin therapeutics bind to bilirubin through the two dipyrromethene moieties, thus highlighting the potential therapeutic impact of these dipyrromethene moieties. Here, we report the synthesis and characterization of two bilirubin biomimetic copper complexes, **CuL1** and **CuL2**, featuring tetrahedral dipyrromethene moieties. DNA binding studies reveal significant affinities for both complexes, with **CuL1** displaying a log K_a of 4.70 ± 0.02, with a corresponding Gibbs free energy change (ΔG) of –26.8 kJ/mol at 25 °C, indicating a moderate-to-high DNA affinity. **CuL2** showed a slightly higher affinity with log K_a of 4.88 ± 0.02, with a corresponding ΔG of –27.4 kJ/mol at 25 °C. These experimental findings aligned closely with computational docking G-scores, which yielded –32.9 kJ/mol for **CuL1** and –34.8 kJ/mol for **CuL2**, respectively. Viscosity, gel electrophoresis, and absorption studies support an intercalative binding mechanism, which was further confirmed by computational docking and molecular dynamics simulations. These findings suggest that copper dipyrromethene complexes may exert therapeutic effects through DNA interaction, warranting further investigation involving *in vitro* cell cultures for drug development potential.

1. Introduction

Bilirubin is a linear tetrapyrrolic biological chromophore produced through the stepwise catabolism of heme (Fig. 1**a**) in ageing red blood cells. Through a series of physiological processes, metal-free bilirubin (Fig. 1**b**) is then eliminated as a waste product. Interestingly, however, bilirubin has demonstrated potent antioxidant features and is gaining popularity as a therapeutic agent [1–5]. These features have consequently lead to bilirubin being exploited in drug development applications, particularly when complexed to a range of metal ions [1–5]. A study conducted found that upon the formation of a bilirubin Cu(II) complex (Fig. 1**c**), Cu(II) was reduced to Cu(I) which resulted in the formation of reactive oxygen species (ROS) identified to be the hydroxyl radical. This reaction was found to cause strand breakages and cleavage in calf thymus DNA as well as in supercoiled plasmid DNA [6,7]. It has been suggested that the metal ion binds to bilirubin through the dipyrromethene moieties; these dipyrromethene moieties are therefore of therapeutic interest [8–11].

Derivatives and complexes of dipyrromethenes [12] find use in numerous applications such as dyes [13], photovoltaics [14], sensors [15], and therapeutics [16]. Reported rhodium, ruthenium, and iridium dipyrromethene metal complexes have been reported to bind to DNA [17,18]. Both groove binding and intercalation have been reported for these complexes with binding constants (K_b) varying across the range of 6.3×10^{-4} to 2.3×10^{-5} M^{-1} or log K 3.2 to 4.6 [13,14]. Their cytotoxicity was also evaluated in Dalton's Lymphoma cancer cell lines and the half-maximal inhibitory concentration (IC_{50}) value varied between the different compounds over the range 5–100 μg/mL, with the most cytotoxic compound having a low IC_{50} value of 5–10 μg/mL [13].

The identity of the metal ion and substituents on the dipyrrin ligands are integral to the various geometries and complexation behaviour exhibited by dipyrrinato-complexes [12]. These geometries then relate directly to whether a complex is going to be a DNA binder and the type of binding possible [19–21].

Copper is a trace element that plays a vital role in various physiological processes [22] including redox reactions, energy metabolism, and DNA synthesis [23]. It is a constituent of essential enzymes such as cytochrome oxidase, tyrosinase, and superoxide dismutase [24,25], underscoring its significance in maintaining cellular function and overall health. Notably, tumour cells also exhibit a high demand for

* Corresponding authors.
E-mail addresses: matthewbracken125@gmail.com (M.L. Bracken), sadhna.mathura@wits.ac.za (S. Mathura).

https://doi.org/10.1016/j.poly.2024.117161
Received 16 April 2024; Accepted 25 July 2024
Available online 26 July 2024

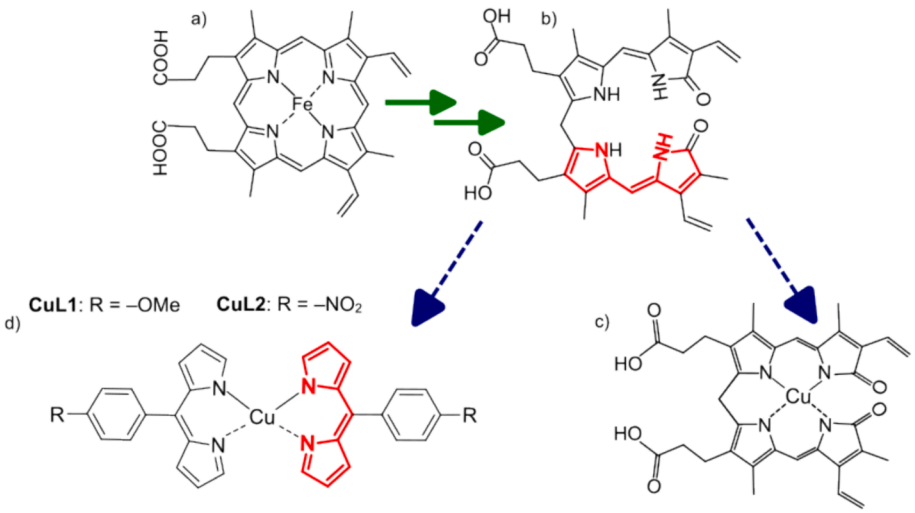

Fig. 1. A proposed structure of a Cu(II) bilirubin complex a). The general structure of the dipyrromethene copper complexes synthesised in this work b) with the recurring dipyrromethene motif highlighted in red. **CuL1** refers to the complex formed when the R group in the *meso* position is –OMe and **CuL2** refers to the complex formed when the R group in the *meso* position is $–NO_2$. ((Colour online.))

copper [25], suggesting that novel copper compounds could potentially serve as anti-cancer agents and provide an alternative to the more commonly employed platinum-based compounds [17,19].

The development of copper-based anti-cancer drugs has garnered significant attention in recent years [23,25–32]. These copper complexes have exhibited cytotoxicity against various cancer cell lines, including those resistant to traditional chemotherapy, and have demonstrated the ability to overcome multidrug resistance [32]. The mechanisms of action of copper complexes include the catalysis of reactive oxygen species (ROS) production [22,24,25,27,32,33]. Additionally, copper complexes have been shown to act as effective DNA binding and cleavage agents [22,27,29,33,34], contributing to their therapeutic efficacy. Importantly, the endogenous presence of copper suggests potential reduced toxicity towards normal cells relative to cancer cells, making copper-containing metallodrugs a suitable option as anti-cancer therapeutics [23,29].

In this study, *meso*-substituted copper dipyrromethene complexes (Fig. 1**d**) were synthesised, characterised, and their DNA binding ability was evaluated by a combination of spectroscopy, viscometry, gel electrophoresis and molecular docking studies.

2. Experimental

2.1. Chemicals and instrumentation

All chemicals were purchased from Sigma-Aldrich and used without further purification. All solvents were purchased from Merck, and when necessary, freshly distilled. NMR data were acquired on Bruker Avance III 400 or Avance III 300 NMR spectrometers at frequencies of 400 MHz or 300 MHz (^{1}H), respectively, and 100 MHz or 75 MHz (^{13}C), respectively, using either a 5 mm BBOZ probe or a 5 mm TBIZ probe. All proton and carbon chemical shifts are quoted relative to the relevant solvent reference signal. Spectra were analysed with MestReNova (Version 12.0.0–20080). Data were acquired at a temperature of 300 K. Infrared spectra of powder samples were recorded using a Bruker Alpha FTIR spectrometer using a Bruker Platinum diamond Attenuated Total Reflectance sampling accessory. OPUS software (Version 7.5) was used to analyse spectra. The spectra were acquired over 24 scans at 20 °C with a spectral resolution of 4 cm^{-1}. UV–Vis absorbance spectra were recorded at 25 °C using a Specord 210® Plus (Analytik Jena) using WinASPECT Plus version 4.2.0.0. The temperature was controlled by an external thermostatted circulating water bath and water-circulating cell holders. Crystal data were collected on a Bruker D8 Venture Bio PHOTON III diffractometer with a MoKα Iμ DIAMOND source (50 kV, 1.4 mA). The collection method involved ω- and φ-scans with 1536 × 1024 (PHOTON III) bit data frames. The unit cell and full data set were collected using APEX4 [35]; SAINT was used to integrate the data, and SADABS was used to make empirical absorption corrections and scale the data. Space group assignments were made using XPREP on all compounds. Using Olex2 [36], the crystal structures were solved with the ShelXT [37] structure solution program using Intrinsic Phasing and refined with the ShelXL [38] refinement package using Least Squares minimization. Non-hydrogen atoms were first refined isotropically followed by anisotropic refinement by full-matrix least-squares calculations based on F^2.

2.2. Synthesis

Dipyrromethanes (L1a and L2a) were synthesised by a modified procedure [39,40]. From L1a and L2a, dipyrromethenes (L1 and L2) and their corresponding metal complexes (**CuL1** and **CuL2**) were synthesised from a modified procedure that was previously reported [41].

2.2.1. Synthesis of 5-(4-methoxyphenyl)dipyrromethane, L1a

To 100 mL of 0.18 M aqueous HCl solution, freshly distilled pyrrole (1.7 mL, 24 mmol, 3 eq.) was added, followed by the addition of 4-anisaldehyde (1.0 mL, 8.2 mmol, 1 eq.). The reaction mixture was stirred at room temperature in the dark overnight. The crude product was extracted with EtOAc (3 x 50 mL). The organic fraction was dried using $MgSO_4$, filtered through celite and then evaporated under reduced pressure. The product was purified by column chromatography [silica, petroleum ether/chloroform (80:20)] to afford a yellow oil. The product was then recrystallised from MeOH/H_2O to afford a tan-coloured solid, which is 5-(4-methoxyphenyl)dipyrromethane (722 mg, 35 %).

^{1}H NMR (400 MHz, DMSO-d_6) [δ, ppm]: 10.02 (br, 2H), 7.07 (d, 2H, J=8.8 Hz), 6.84 (d, 2H, J=8.7 Hz), 6.60 (m, 2H), 5.89 (m, 2H), 5.63 (m, 2H), 5.29 (s, 1H), 3.71 (s, 3H). ^{13}C NMR (100 MHz, DMSO-d_6) [δ, ppm]: 42.67, 55.06, 105.90, 106.82, 113.42, 116.75, 129.07, 133.54, 135.92, 157.63. FTIR (cm^{-1}): 3339.79, 1609.60, 1510.71, 1301.90, 1252.05, 1175.09, 1110.67, 1031.19. UV/vis (CH_3CN) [λ max (nm), ε ($M^{-1}cm^{-1}$)]: 225, 2.37 x 10^4; 280, 2.20 x 10^3.

2.2.2. Synthesis of 5-(4-nitrophenyl)dipyrromethane, L2a

To 100 mL of 0.18 M aqueous HCl solution, freshly distilled pyrrole (1.30 mL, 19 mmol, 3 eq.) was added, followed by the addition of 4-nitrobenzaldehyde (942 mg, 6.2 mmol, 1 eq.). The reaction mixture

was stirred at room temperature in the dark for 2 h. The precipitated product was filtered off and washed with water and then petroleum ether before being dried under vacuum. The product was purified by column chromatography [silica, EtOAc/hexane (20:80)] to afford a yellow solid which is 5-(4-nitrophenyl)dipyrromethane (892 mg, 54 %).

^{1}H NMR (400 MHz, DMSO-d_6) [δ, ppm]: 10.68 (s, 2H), 8.18 (d, 2H, J=8.7 Hz), 7.41 (d, 2H, J=8.7 Hz) 6.65 (m, 2H), 5.94 (m, 2H), 5.69 (s, 2H), 5.54 (s, 1H). ^{13}C NMR (100 MHz, DMSO-d_6) [δ, ppm]: 43.44, 106.55, 107.20, 117.42, 123.46, 129.36, 131.77, 145.99, 151.69. FTIR (cm^{-1}): 3355.19, 1509.53, 1342.91, 1113.00, 1027.99. UV/vis (CH_3CN) [λ max (nm), ε ($M^{-1}cm^{-1}$)]: 269, 2.81 x 10^4.

2.2.3. Synthesis of 5-(4-methoxyphenyl)dipyrromethene, L1

A solution of DDQ (114 mg, 0.502 mmol, 1.1 eq.) dissolved in THF (5 mL) was added to a solution of **L1a** (115 mg, 0.456 mmol, 1 eq.) dissolved in 5 mL of THF. The reaction mixture was purged with argon for 5 min before being sealed and stirred at room temperature for 2 h. TLC analysis [silica, chloroform: hexane (1:1)] after 2 h showed complete consumption of starting material. The solvent was removed under reduced pressure and the residue was dissolved in CH_2Cl_2 prior to a water/brine wash. The crude product was extracted with CH_2Cl_2 (3 x 10 mL). The organic fraction was dried with $MgSO_4$, filtered through celite and concentrated under reduced pressure to afford a reddish brown residue which was then purified by column chromatography [silica, chloroform: hexane (1:1)] which afforded a brown-yellow solid of 5-(4-methoxyphenyl)dipyrromethene, **L1** (54 mg, 47 %).

^{1}H NMR (300 MHz, DMSO-d_6) [δ, ppm]: 8.07 (s, 2H), 7.52 (d, 2H, J=8.7 Hz), 7.20 (d, 2H, J=8.7 Hz), 6.79 (s, 2H), 3.92 (s, 3H). ^{13}C NMR (75 MHz, DMSO-d_6) [δ, ppm]: 56.26, 98.63, 115.03, 116.91, 118.50, 130.99, 132.01, 136.50, 142.57. FTIR (cm^{-1}): 2922.08, 2852.10, 2230.49, 1599.91, 1567.32, 1464.40, 1343.88, 1265.75. UV/vis (CH_3CN) [λ max (nm), ε ($M^{-1}cm^{-1}$)]: 435, 1.48 x 10^4; 478, 2.05 x 10^4.

2.2.4. Synthesis of 5-(4-nitrophenyl)dipyrromethene, L2

A solution of DDQ (110 mg, 0.485 mmol, 1.1 eq.) dissolved in THF (5 mL) was added to a solution of **L2a** (113 mg, 0.423 mmol, 1 eq.) dissolved in 5 mL of THF. The reaction mixture was purged with argon for 5 min before being sealed and stirred at room temperature for 2 h. TLC analysis [silica, chloroform: hexane (1:1)] after 2 h showed complete consumption of starting material. The solvent was removed and the residue was dissolved in CH_2Cl_2 prior to a water/brine wash. The crude product was extracted with CH_2Cl_2 (3 x 10 mL). The organic fraction was dried with $MgSO_4$, before being filtered through celite to afford a reddish brown residue. This material was purified by column chromatography [silica, EtOAc: hexane (1:1)] which afforded a brown-yellow solid of 5-(4-nitrophenyl)dipyrromethene, **L2** (68 mg, 61 %).

^{1}H NMR (400 MHz, $CDCl_3$) [δ, ppm]: 14.57 (br, 1H), 8.33 (d, 2H, J=8.4 Hz), 8.08 (s, 2H), 7.60 (d, 2H, J=8.4 Hz), 6.58 (d, 4H, J=10.8 Hz). ^{13}C NMR (100 MHz, $CDCl_3$) [δ, ppm]: 29.71, 117.98, 123.12, 131.83, 136.27, 145.28. FTIR (cm^{-1}): 2919.70, 1809.17, 1559.39, 1516.35, 1451.81, 1342.79, 1168.17, 1044.20. UV/vis (CH_3CN) [λ max (nm), ε ($M^{-1}cm^{-1}$)]: 363, 6.05 x 10^3; 444, 6.1 x 10^3.

2.2.5. Synthesis of CuL1

L1 (36.0 mg, 0.144 mmol, 1 eq.) was dissolved in 20 mL of warm MeOH followed by the addition of $Cu(OAc)_2 \bullet H_2O$ (146.6 mg, 0.734 mmol, 6 eq.) dissolved in 4 mL of a 10 % ammoniacal MeOH solution. The reaction was allowed to stir at room temperature overnight. The green precipitated product was then filtered and washed with 2 mL of MeOH. This material was then dissolved in chloroform and filtered through a short plug of silica. The filtrate was concentrated to afford **CuL1** (18 mg, 23 % yield). Crystals suitable for X-ray diffraction were grown over 48 h by layering a concentrated solution of chloroform with hexane.

FTIR (cm^{-1}): 3361.59, 3171.89, 2204.63, 1603.26, 1536.35, 1429.27, 1231.22, 1022.59, 889.04. UV/vis (DMSO) [λ max (nm), ε ($M^{-1}cm^{-1}$)]: 350, 2.00 x 10^4; 493, 3.21 x 10^4. Crystal Data for $C_{32}H_{26}CuN_4O_2$ (M=562.11 g/mol): tetragonal, space group $P4_12_12$ (no. 92), a = 8.8707(4) Å, c = 63.605(5) Å, V=5005.1(6) Å^3, Z=8, T=173.0 K, μ(MoKα) = 0.912 mm^{-1}, D_{calc} = 1.492 g/cm^3, 197,922 reflections measured (4.636° ≤ 2Θ ≤ 52.718°), 5090 unique (R_{int} = 0.0975, R_{sigma} = 0.0362) which were used in all calculations. The final R_1 was 0.0738 (I>2σ(I)) and wR_2 was 0.1744 (all data).

2.2.6. Synthesis of CuL2

L2 (31.6 mg, 0.119 mmol, 1 eq.) was dissolved in 10 mL of warm MeOH followed by the addition of $Cu(OAc)_2 \bullet H_2O$ (120.6 mg, 0.604 mmol, 6 eq.) dissolved in 3 mL of a 10 % ammoniacal MeOH solution. The reaction was allowed to stir at room temperature for 4 h before the precipitated dark red–black product was filtered and washed with 2 mL of MeOH. The material was then dissolved in chloroform and filtered through a short plug of silica. Upon evaporation of the filtrate, pleochroic red-green crystals of **CuL2** suitable for X-ray diffraction were obtained (12.2 mg, 17 % yield).

FTIR (cm^{-1}): 2920.39, 2851.14, 1595.30, 1541.05, 1374.08, 1326.86, 1235.75, 1172.37, 1015.94, 986.52. UV/vis (CH_3CN) [λ max (nm), ε ($M^{-1}cm^{-1}$)]: 271, 9.60 x 10^3; 317, 7.68 x 10^3; 474, 1.97 x 10^4. Crystal Data for $C_{30}H_{20}CuN_6O_4$ (M=592.06 g/mol): orthorhombic, space group $Ccce$ (no. 68), a = 32.493(9) Å, b = 10.209(3) Å, c = 7.580 (2) Å, V=2514.5(11) Å^3, Z=4, T=123.0 K, μ(MoKα) = 0.920 mm^{-1}, D_{calc} = 1.564 g/cm^3, 15,469 reflections measured (5.014° ≤ 2Θ ≤ 50°), 1109 unique (R_{int} = 0.2168, R_{sigma} = 0.0919) which were used in all calculations. The final R_1 was 0.0799 (I>2σ(I)) and wR_2 was 0.2013 (all data).

2.3. DNA binding

Absorbance spectra were recorded at 25 °C using a Specord 210® Plus (Analytik Jena) using WinASPECT Plus version 4.2.0.0. Spectra were recorded from 250-900 nm, at 50.0 nm/s. The copper complexes were prepared in 150 mM MOPS aqueous buffer with 10 % (v/v) DMSO at pH 7.4. The copper complex concentration was kept constant at 16.6 μM for **CuL1** and 18.2 μM for **CuL2**. The titration was recorded in triplicate and performed by adding aliquots of ctDNA in 150 mM MOPS aqueous buffer with 10 % (v/v) DMSO at pH 7.4 to the copper complex solution. The recorded data was corrected for with the blank, baseline and appropriate dilution factor.

2.4. Viscosity

All viscometric analyses were carried out using an Anton Paar Lovis 2000 M rolling ball microviscometer. Measurements were made in triplicate as a function of the concentration of Cu(II) chelate added to a fixed concentration of ctDNA (50 μM) at 25 °C in 150 mM MOPS aqueous buffer at pH 7.4 with 10 % (v/v) DMSO. Samples were incubated at 37 °C for 30 min before measurement. The average viscosity data are presented as a normalized graph of $(\eta/\eta_0)^{1/3}$ versus the concentration of compound divided by the concentration of ctDNA, where η and η_0 are the dynamic viscosities in the presence and absence of compound, respectively.

2.5. Agarose gel electrophoresis

Gel electrophoresis experiments were carried out using hand-cast 1 % agarose gels dissolved in 1x TA buffer (Sigma-Aldrich, 10x, diluted with Type 1 ultrapure water, 40 mM Tris-acetate; pH 7.4) in a Mini-Sub-Cell GT® Agarose Gel Electrophoresis System (Bio-Rad). The samples were prepared with a constant concentration of ctDNA (40 μM) in 1xTA buffer (pH 7.4) with 5 % (v/v) DMSO. The samples were incubated at 37 °C for 30 min. A loading dye (Sigma-Aldrich, 6X, containing 0.25 % bromophenol blue, 0.25 % xylene cyanol and 40 % sucrose) was added prior to the samples being loaded onto the gel, which was run at 75 V

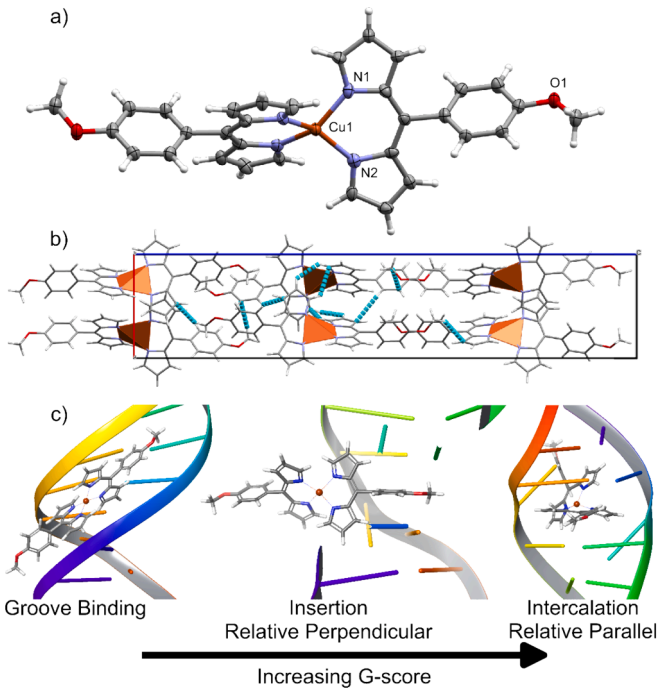

Fig. 2. a) ORTEP diagram of **CuL1**. Packing has been shown in b) as viewed parallel to the crystallographic *b*-axis with metal centres shown as tetrahedra. Hypothetical binding modes to DNA as determined by docking are shown in c).

and 400 mAh for 90 min. The gels were stained with an ethidium bromide solution (0.5 mg/L in Type 1 ultrapure water) for 25 min, washed in Type 1 ultrapure water for 25 min and visualized using an Invitrogen dual LED Blue/White Light Transilluminator.

2.6. DNA thermal denaturation studies

DNA thermal denaturation experiments were recorded in duplicate using a 1.00 cm path length quartz cell, with concentrations of the ctDNA and the compounds at 15 μM. The samples were prepared in 150 mM MOPS aqueous buffer with 10 % (v/v) acetonitrile at pH 7.4. Measurements at 260 nm were recorded at 10 °C intervals between 20 °C and 60 °C, 5 °C intervals between 60 °C and 70 °C and 2 °C intervals between 70 °C and 90 °C. Data were corrected and normalized, and the temperature at which 50 % of the DNA was denatured was determined from the resultant graph. Electronic spectra were recorded with a PerkinElmer UV/VIS Lambda 365 spectrometer fitted with a Peltier Temp. multicell unit and Peltier controller. Quartz cuvettes with 10 mm pathlength were used. UV Express software (Version 4.1.2) was used to analyse spectra.

2.7. Computational chemistry

2.7.1. Density functional theory

All simulations were performed using Gaussian 16 Rev C.01 [42]. Optimization was calculated for **CuL1** and **CuL2** at the CAM-B3LYP [43] /LANL2DZ [44] level of theory, utilizing a large basis set and dispersion-corrected functional for improved accuracy. All simulations were carried out *in vacuo* and GaussView 6.0.16 [45] was used to prepare input files and visualize output data. Time-dependent DFT (TD-DFT) calculations were performed at the same level of theory to simulate the UV–vis spectra of **CuL1** and **CuL2**. A water solvent continua model (Self-Consistent Reaction Field) [46] was applied as necessary, and only 60 excited singlet states were computed to give good overlap with experimental spectra.

2.7.2. Molecular docking & dynamics

2.7.2.1. Ligand preparation. The metal chelates used for docking were first optimized with DFT at the CAM-B3LYP/LANL2DZ level of theory to determine the likely coordination geometry at the metal center and ligand conformation. The DFT-optimized structures were then subjected to optimization using the OPLS2005 force field with standard parameters for LigPrep (LigPrep, Schrödinger, LLC, New York, NY, USA, 2021). This was done to generate files associated with Schrödinger. The force field was not parameterized for the metal chelates under study and it was thus necessary to apply zero-order bonds between the metal ion and the organic framework. The force field then treats the metal–ligand bonds using parameterized electrostatic forces, ignoring the covalent nature of the metal–ligand bond. This is necessary to dock metal complexes using Schrödinger.

2.7.2.2. DNA preparation. The X-ray structures of DNA were solved to a final resolution of 2.80 Å (PDB:425D) [47] and 0.92 Å (PDB: 4E1U) [48] and retrieved for preparation using the Protein Preparation Wizard [49] employed in the Schrödinger Suite 2020–4. The structure contains co-crystallised water molecules or ligands. The DNA was selected, and the selection was inverted before deleting all components of the crystal save a single DNA macromolecule. The structures were pre-processed at pH 7.4 using Epik [50] to generate heteroatom ionization states. The missing terminal phosphate backbones were then added in Maestro. The hydrogen-bond assignment was optimized at pH 7.4 and restrained minimization was performed using the OPLS2005 [51] force field converging heavy atoms to a root-mean-square deviation (RMSD) of 0.30 Å. PDB:425D is suitable for generating groove binding poses while PDB:4E1U is ideal for generating intercalated docking poses.

2.7.2.3. Ligand docking. The prepared ligands were docked into DNA using Glide [52] to identify potential binding sites for the metal chelates on the genetic material. The receptor grid was centred on nucleobases close to the centre of the DNA strand with dimensions 40 × 40 × 40 $Å^3$ so that all of the DNA was sampled for potential binding sites. XP(extra precision) [53] docking was then used to generate binding poses on the DNA.

2.7.2.4. Molecular dynamics. Molecular dynamics (MD) simulations were performed on the best-docked DNA-ligand complexes using Desmond [54] and the OPLS2005 force field. The DNA–ligand complexes were already pre-processed before the System Builder in Desmond was used to solvate the system with TIP3P [55] water molecules. The biomolecular system was placed in an orthorhombic box with a buffer region of 5 Å between the box boundary and the DNA–ligand complex and then neutralized with Na^+ as necessary. The simulation times were set to 100 ns and the approximate number of frames was kept constant at 1000 so that the recording interval was 100 ps. The model system was relaxed before simulation, and equilibration was performed using the NPT [56] ensemble at 310 K and 1.01 bar. The trajectories were then analyzed in Maestro.

3. Results and discussion

3.1. Crystallography

The crystal data for **CuL1** and **CuL2** have been presented in the experimental section and CIF files are available as part of the Supporting Information. **CuL1** crystallized in the tetragonal space group $P4_12_12$ with 8 molecules in the unit cell. **CuL1** is shown Fig. 2**a** with 50 % ellipsoid probability and hydrogen atoms as fixed spheres of radius 0.15 Å. The Cu(II) centre is 4-coordinate with distorted tetrahedral geometry. The inner coordination sphere comprises of four pyrrole nitrogen donors, two neutral nitrogen donors from 2*H*-pyrrole, and two anionic

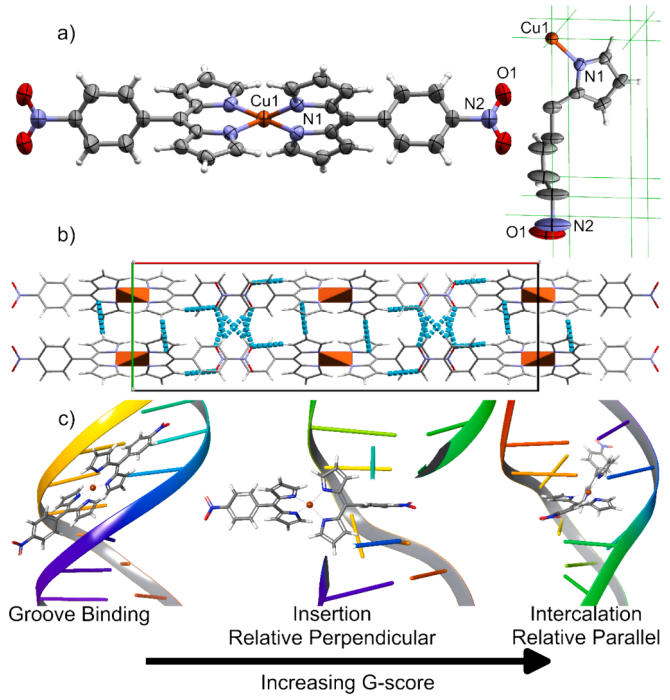

Fig. 3. a) ORTEP diagram of **CuL2** along with the asymmetric unit. Due to the high symmetry of the space group, the bond lengths of **CuL2** are solved as a positional average. Packing has been shown in b) as viewed parallel to the crystallographic *c*-axis with metal centres shown as tetrahedra. Hypothetical binding modes to DNA as determined by docking are shown in c).

nitrogen donors from the deprotonation of 1*H*-pyrrole. The anionic donors, N1, are arranged trans to the neutral donors, N2. This relieves interelectronic repulsion at the metal centre as the anionic electron density is delocalized into π-acceptor orbitals located on the C═N moiety of the 2*H*-pyrrole rings. With respect to a perfect tetrahedron, which exhibits a dihedral angle of 90° between its planes as depicted in Fig. 4**a**, the dihedral angle calculated between the *N*-Cu-N planes were found to be 48.55° for **CuL1** as illustrated in Fig. 4**b** which highlights the distortion from an ideal tetrahedron for **CuL1**. The packing of **CuL1** is shown in Fig. 2**b** and the unit cell is viewed parallel to the crystallographic *b*-axis. The intermolecular forces that facilitate packing are dominated by C—H ··· π interactions which have been shown as blue cylinders. These C—H ··· π interactions exist between methyl hydrogens and the benzene rings on adjacent chelates, as well as between methyl hydrogens and the π-system on neighbouring pyrrole rings. Additional C—H ··· π interactions exist between benzene hydrogens and adjacent pyrrole rings. Due to these packing effects, the benzene rings and pyrrole rings are orientated relative perpendicular. However, in solution, there is free-rotation and the aromatic rings may orientate relative parallel for optimal insertion into DNA. This has been shown by docking in Fig. 2**c**. The tetrahedral geometry of the Cu(II) chelate is ideal for initial groove binding on the DNA, it is then hypothesized that displacement of stacked nucleobase pairs allows the chelate to insert DNA with the aromatic rings of the ligand orientated relative perpendicular. As the Cu(II) complex stabilises, the aromatic rings orientate relative parallel for optimal intercalation with DNA. These binding modes, initial groove binding, followed by insertion and ultimately intercalation, show progressively higher docking scores.

CuL2 crystallized in the orthorhombic space group *Ccce* with 4 molecules in the unit cell. **CuL2** is shown Fig. 3**a** with 50 % ellipsoid probability and hydrogen atoms as fixed spheres of radius 0.15 Å; the asymmetric unit is also shown. The Cu(II) centre is 4-coordinate with distorted tetrahedral geometry. The inner coordination sphere comprises of four pyrrole nitrogen donors, two neutral nitrogen donors from 2*H*-pyrrole, and two anionic nitrogen donors from the deprotonation of 1*H*-pyrrole. Because the metal-centre of the asymmetric unit lies on two symmetrical 2-fold rotational axes, the bond lengths are solved as a positional average and hence anionic and neutral donors cannot be discriminated. In reference to the tetrahedral geometry, With respect to a perfect tetrahedron, which exhibits a dihedral angle of 90° between its planes as depicted in Fig. 4**a**, the dihedral angle calculated between the *N*-Cu-N planes were found to be 49.31° for **CuL2** as illustrated in Fig. 4**c** which highlights the distortion from an ideal tetrahedron for **CuL2**.The packing of **CuL2** has been shown in Fig. 3**b** and the unit cell is viewed parallel to the crystallographic *c*-axis. The intermolecular forces that facilitate packing are dominated by C—H···π and C—H···O interactions between adjacent nitrobenzene rings. There are also C—H···π and C—H···O interactions between pyrrole rings and neighbouring nitrobenzene rings. This is in contrast to **CuL1,** which only contains C—H···π interactions due to the absence of the nitro group. This has a significant effect on the solubility of the chelates as **CuL1** remains in aqueous solution whilst **CuL2** will precipitate from solution over 48 h. These intermolecular interactions impose a relative perpendicular orientation

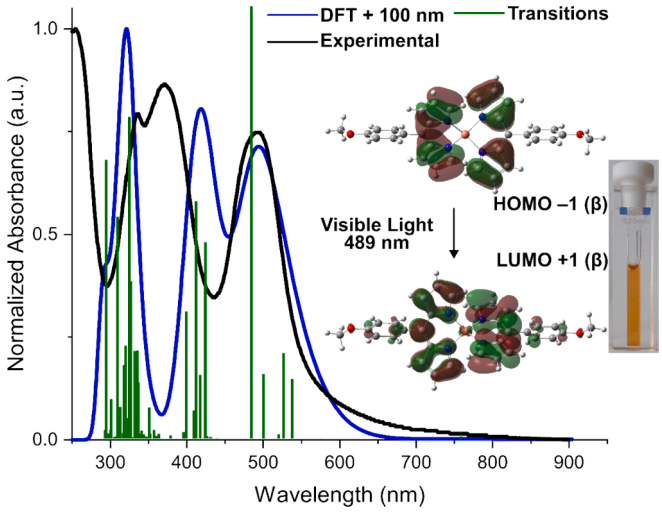

Fig. 5. The experimental and DFT calculated UV–Vis spectra of **CuL1** as well as 60 excited singlet state transitions. The dominant electronic transition responsible for the visible colour of the **CuL1** solution was calculated at 489 nm and observed at 493 nm. Spectra normalized for comparison.

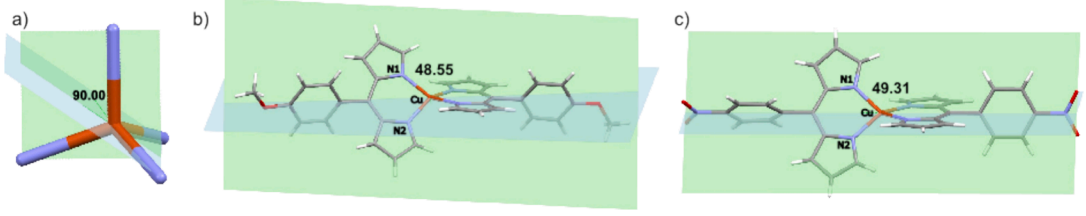

Fig. 4. a) Dihedral angle calculated for a perfect tetrahedron. dihedral angles calculated between the planes that pass through two pyrrole nitrogen atoms bonded to the central copper atom (*N*-Cu-N plane) for b) **CuL1** and c) **CuL2**.

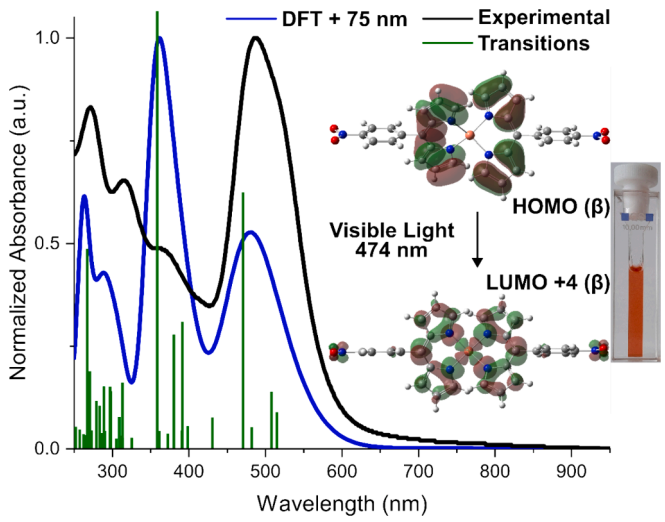

Fig. 6. The experimental and DFT calculated UV–Vis spectra of **CuL2** as well as 60 excited singlet state transitions. The dominant electronic transition responsible for the visible colour of the **CuL2** solution was calculated at 474 nm and observed at 488 nm. Spectra normalized for comparison.

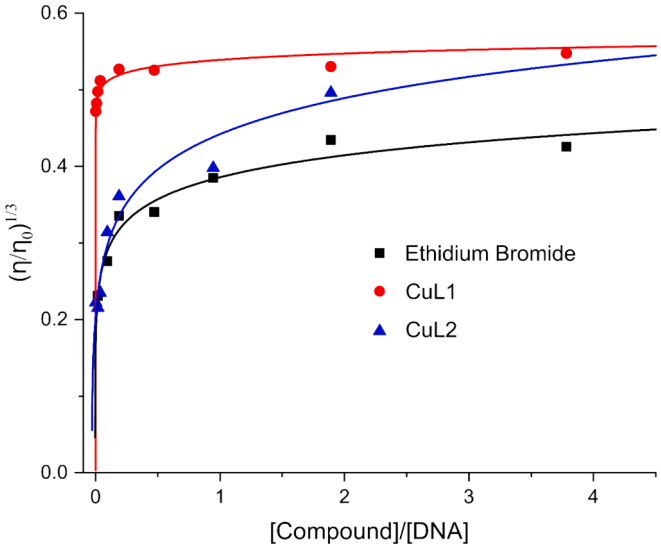

Fig. 7. Average viscosity data is presented as a normalised graph of $(\eta/\eta_o)^{1/3}$ against value of the concentration of the compound divided by the concentration of ctDNA. η and η_o are the dynamic viscosities in the presence and absence of compound, respectively. The viscosity data for ethidium bromide, a known DNA intercalator is represented in black. The viscosity data for **CuL1** and **CuL2** is represented in red and blue, respectively. ((Colour online.))

for aromatic rings on the ligand. However, in solution, there is free-rotation and the aromatic rings may orientate relative parallel for optimal insertion into DNA. This has been shown by docking in Fig. 3**c**. The hypothetical DNA binding interaction is similar for **CuL1** and **CuL2**, however **CuL2** produces consistently higher G-scores compared to **CuL1**. The binding modes, initial groove binding, followed by insertion and ultimately intercalation, show progressively higher docking scores for **CuL2**.

3.2. UV–Vis

UV–vis absorption spectra were recorded in aqueous MOPS buffer at pH 7.4 for **CuL1** and **CuL2**. The experimental spectrum for **CuL1** in aqueous solution is presented in Fig. 5 along with the DFT calculated

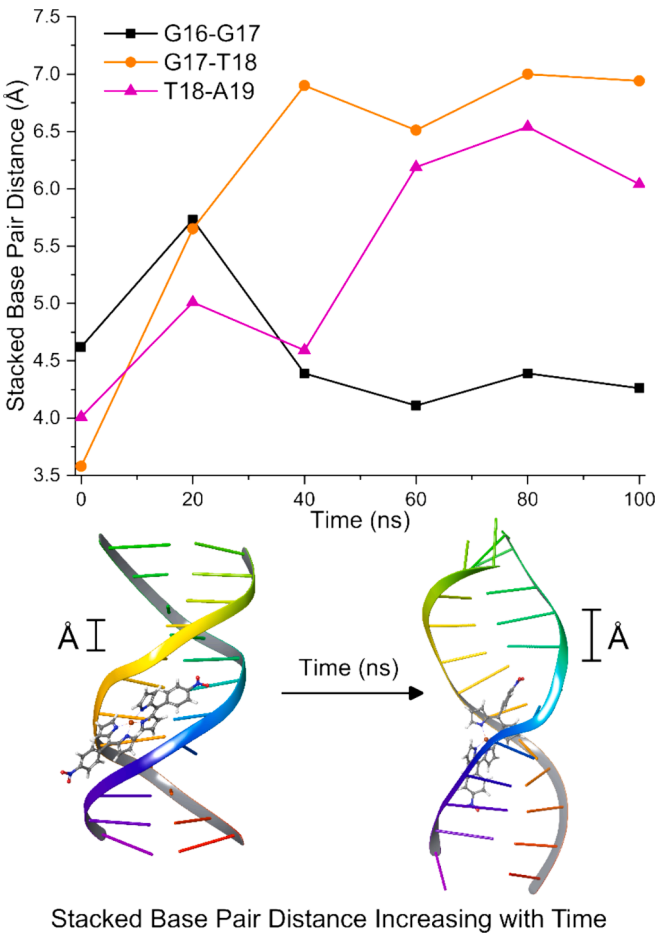

Fig. 8. Stacked base pair distance of DNA bound by **CuL2** over 100 ns molecular dynamics simulation. At time 0 ns, **CuL2** is bound in the minor groove of the DNA. As time progresses, the stacked base pairs become displaced which culminates in DNA insertion. This displacement of base pairs is observed experimentally as the viscosity of the DNA solution increases with increasing chelate concentration. Nucleobases have their usual abbreviations, i.e., G=guanine, A=adenine, T=thymine.

spectrum and the 60 excited state transitions. The absorption band in the visible region at 493 nm is responsible for the yellow-orange colour of the solution and was calculated at 489 nm. This transition at 489 nm was decomposed into the following major contributions: HOMO–1(β)→ LUMO+1(β) (25 %); HOMO(β)→ LUMO+2(β) (24 %); HOMO(α)→ LUMO+1(α) (19 %); and HOMO–1(α)→ LUMO(α) (18 %). The dominant contribution, HOMO–1(β)→ LUMO+1(β), has been shown in Fig. 5 and this π-π* transition involves mostly intraligand charge transfer with some ligand-to-metal character. Moving to higher energy transitions, the experimental absorption at 350 nm was calculated to be 351 nm and this transition involves the following major contributions: HOMO–12(β)→ LUMO(β) (30 %) and HOMO–7(β)→ LUMO+1(β) (29 %). These low-energy HOMOs involve the σ-framework of the ligand whilst the LUMOs have mostly π* character. Hence, the absorption at 350 nm is due to σ-π* transition. **CuL1** also shows experimental UV absorption at 251 nm which was calculated to be 289 nm. This absorption at 289 nm was decomposed into the following major contributions: HOMO(β)→ LUMO+10(β) (23 %); HOMO(α)→ LUMO+9(α) (22 %); and HOMO–1 (β)→ LUMO+12(β) (12 %). These high-energy LUMOs are metal-based and have mostly σ* character. Hence, the absorption at 251 nm is a π-σ* transition with significant ligand-to-metal charge transfer. The UV–vis absorption spectra for **CuL1** and **CuL2** are quite similar in terms of major absorptions *ca.* 500, 350, and 250 nm. The experimental spectrum for **CuL2** in aqueous solution is presented in Fig. 6 along with

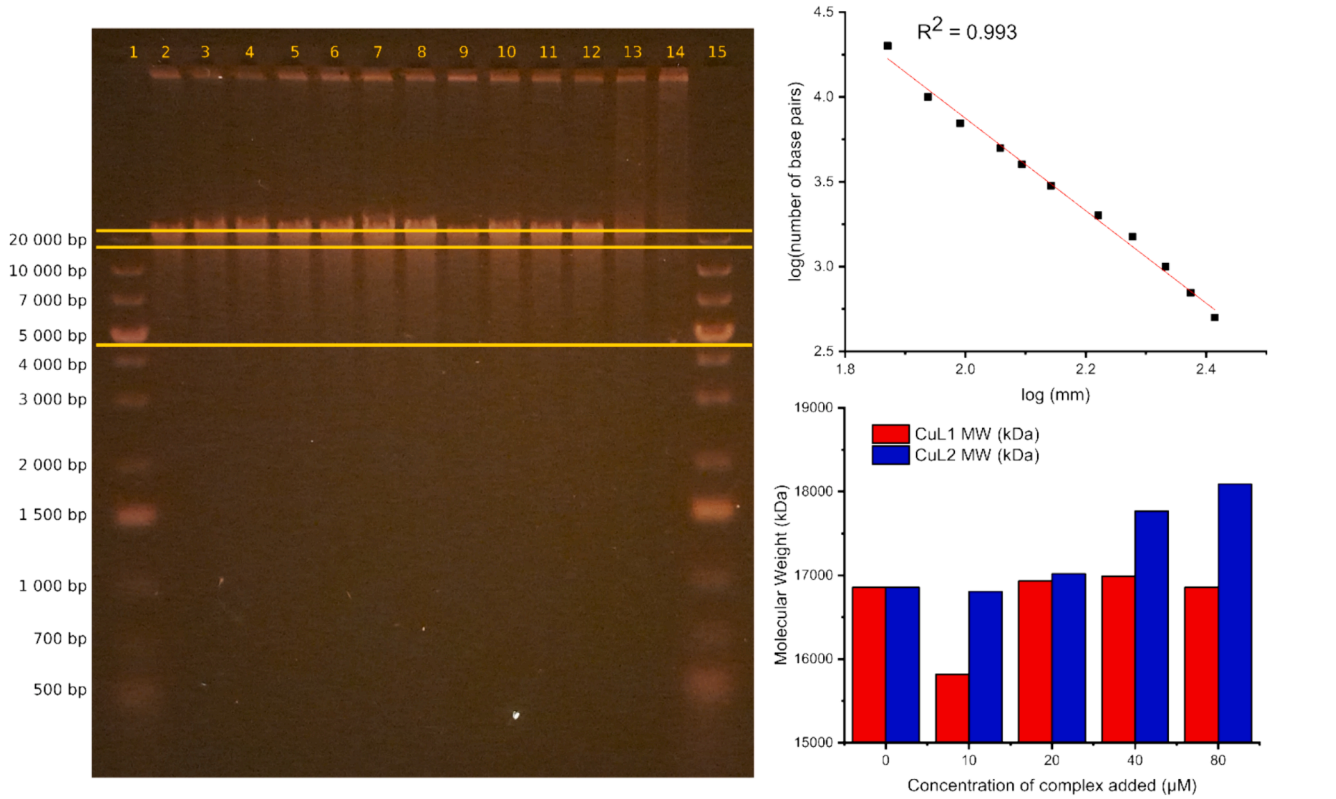

Fig. 9. (Left) DNA binding of agarose gel electrophoresis (1 % agarose) of complexes **CuL1** and **CuL2**. Lane 1—1 kb DNA ladder; lane 2- DNA+DMSO control; lane 3—20 μM EtBr; lane 4—40 μM EtBr; lane 5—10 μM **CuL2**; lane 6—20 μM **CuL2**; lane 7—40 μM **CuL2**, lane 8—80 μM **CuL2**; lane 9—10 μM **CuL1**; lane 10—20 μM **CuL1**; lane 11—40 μM **CuL1**, lane 12—80 μM **CuL1**; lane 13—20 μM Hoechst, lane 14—40 μM Hoechst, lane 15—1 kb DNA ladder. (Top right) Correlation plot using the gene ruler of log distance travelled from the well to the band in mm against the log of the number of base pairs. (Bottom right) Bar graph representing the molecular weight in kDa of **CuL1**-DNA (red) and **CuL2**-DNA (blue) over the concentration range 0—–80 μM. ((Colour online.))

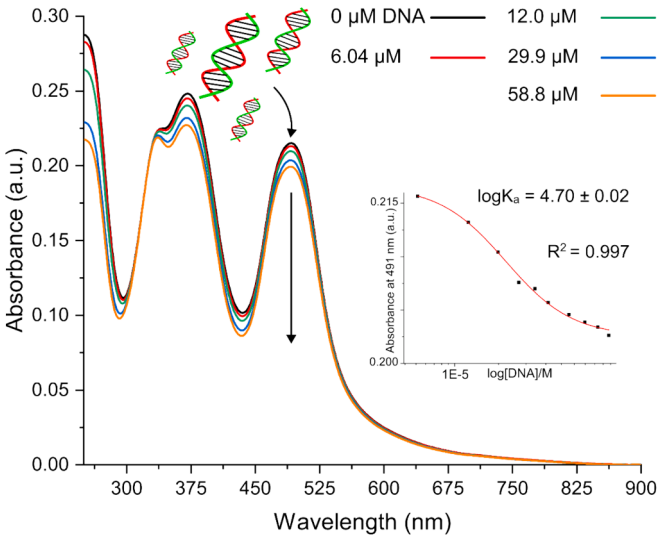

Fig. 10. UV–Vis absorption spectrum of **CuL1** at a constant concentration of 16.6 μM with increasing ctDNA. The Hill equation was plotted with absorbance values at 491 nm and produced a correlation of $R^2 = 0.997$ and a log $K_a = 4.70 \pm 0.02$.

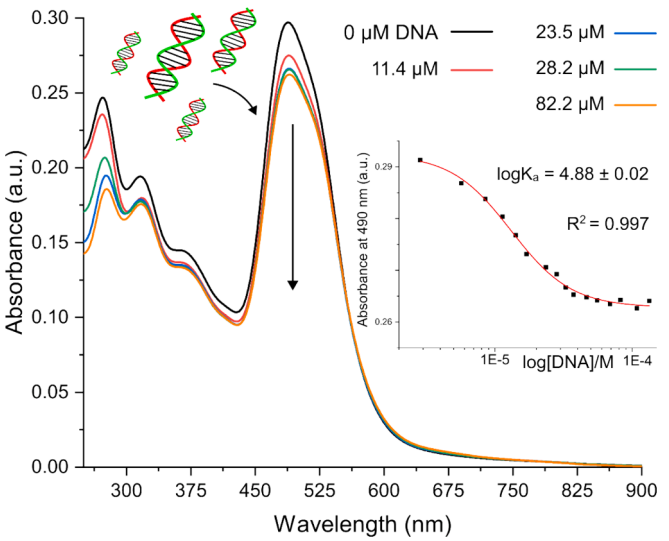

Fig. 11. UV–Vis absorption spectrum of **CuL2** at a constant concentration of 18.2 μM with increasing ctDNA. The Hill equation was plotted with absorbance values at 490 nm and produced a correlation of $R^2 = 0.997$ and a log $K_a = 4.88 \pm 0.02$. The absorption band ca. 275 nm is due to metal–ligand charge transfer and shows a red-shift upon increasing DNA concentration. This indicates that the metal ion is perturbed upon DNA binding and that copper is involved with binding. ((Colour online.))

the DFT calculated spectrum and the 60 excited state transitions. The absorption band in the visible region at 488 nm is responsible for the red–orange colour of the solution and was calculated at 474 nm. This transition at 474 nm was decomposed into the following major contributions: HOMO(β)→ LUMO+4(β) (20 %); HOMO–1(β)→ LUMO(β) (13

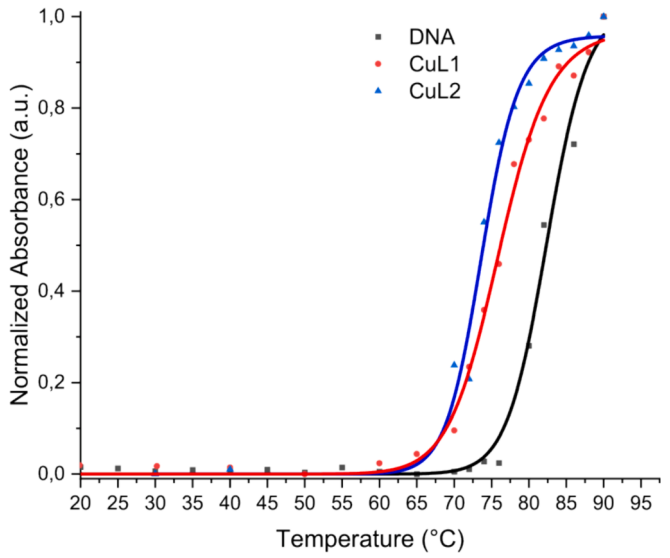

Fig. 12. Thermal denaturation of ctDNA in the absence (black) and presence of 15 μM **CuL1** (red) and 15 μM **CuL2** (blue) in 150 mM MOPS aqueous buffer with 10 % (v/v) acetonitrile at pH 7.4. The ctDNA melt temperature was obtained by the midpoint of the sigmoidal curve. The melt temperatures of ctDNA were as follows: no complex – 82 ± 0.5 °C; **CuL1** – 76 ± 0.3 °C; **CuL2** – 74 ± 0.3 °C. ((Colour online.))

%); HOMO–1(β)→ LUMO+3(β) (12 %); and HOMO(α)→ LUMO+1(α) (10 %). The dominant contribution, HOMO(β)→ LUMO+4(β), has been shown in Fig. 6 and this π-π* transition involves mostly intraligand charge transfer with additional ligand-to-metal character. Moving to higher energy transitions, the experimental absorption at 374 nm was calculated to be 357 nm and this transition involves the following major contributions: HOMO–6(β)→ LUMO(β) (22 %); HOMO–7(α)→ LUMO(α) (21 %); and HOMO–8(α)→ LUMO+1(α) (20 %). These low-energy HOMOs involve non-bonding MOs of the ligand whilst the LUMOs have mostly π* character. Hence, the absorption at 374 nm is due mostly to n-π* transition. **CuL2** also shows experimental UV absorption at 271 nm which was calculated to be 265 nm. This absorption at 265 nm was decomposed into the following major contributions: HOMO(α)→ LUMO+11(α) (20 %); HOMO(β)→ LUMO+12(β) (18 %); and HOMO–1 (β)→ LUMO+14(β) (11 %). These high-energy LUMOs are metal-based and have mostly σ* character. Hence, the absorption at 271 nm is a π-σ* transition with significant ligand-to-metal charge transfer.

3.3. *DNA binding by viscosity, gel electrophoresis, and spectroscopy*

Intercalation of a metal complex to DNA results in increased viscosity of the biochemical solution due to an increase in the length of DNA. The viscosity of the ctDNA metal complex with an increasing concentration of either **CuL1** or **CuL2** were compared against ethidium bromide, which is a known DNA intercalator. As seen in Fig. 7, both **CuL1** and **CuL2** present an increase in viscosity with increasing concentration which indicates that both complexes interact via an intercalative mechanism. The binding of the metal complex between the stacked base pairs of DNA results in an increased distance between those base pairs [57,58]. Because **CuL1** and **CuL2** are larger than ethidium bromide, and the complexes are tetrahedral rather than planar, these chelates cause a larger increase in viscosity than ethidium bromide. We have shown by molecular dynamic (MD) simulations that **CuL2** may initially bind DNA at the minor groove, which causes stacked nucleobases to become displaced and culminates in intercalation. This hypothetical stepwise binding has been presented in Fig. 8. The complex was initially docked onto DNA as a minor groove binder, this system was then subjected to 100 ns MD calculation. Over the simulated time, stacked base-pairs became displaced and **CuL2** was able to insert DNA. Because samples are incubated before experimental viscosity measurements, and the hypothetical stepwise binding occurs on a nanosecond time scale, only intercalation is observed experimentally and is determined to be the primary mechanism. This was further supported by gel electrophoresis as shown in Fig. 9. The molecular weight range of the ctDNA metal complex band is between 20 000–22 000 bp. Both complexes, **CuL1** and **CuL2**, show more similar band patterns to the ethidium bromide (Lanes 3–4) compared to that of the Hoechst stain (lanes 13–14). **CuL2** (lanes 5–8) shows a steady increase in molecular weight of the DNA sample as the concentration of **CuL2** is increased. This indicates that the metal complex has intercalated and bound DNA, thereby increasing the observed mass compared to unbound DNA. Unlike the copper-bilirubin complex that resulted in DNA cleavage [6,7], no cleavage was observed in the gel in Fig. 9. DNA cleavage would result in fragments with varying molecular weights which would present as multiple bands throughout the gel [59,60].

Absorption titration studies were conducted to investigate the interaction between ctDNA to the copper chelates by monitoring the change in absorption intensity in relation to the addition of ctDNA aliquots. If the copper complex interacts with DNA via an intercalative mechanism, hypochromism with a bathochromic shift is observed which is caused by the stacking interaction occurring between the DNA base pairs and an aromatic chromophore. If the binding mode of a complex to DNA is via an electrostatic interaction or a non-intercalative mechanism, hyperchromism is typically observed and this is due to the partial uncoiling of the DNA double helix [61]. The spectra for both **CuL1** and **CuL2** display a decrease in absorption intensity (hypochromism) as shown in Fig. 10 and Fig. 11, respectively. The absorption values at varying DNA concentration were plotted using the Hill equation [62] to determine the binding affinity. **CuL1** produced a binding affinity log K_a = 4.70 ± 0.02 which can be considered moderate-to-high DNA affinity. From equilibrium thermodynamics, ΔG=–RTlnK_a, where all variables have their usual meaning, **CuL1** binds DNA with a favourable Gibbs energy ΔG=–26.8 kJ/mol at 25 °C. **CuL2** produced a slightly higher binding affinity log K_a = 4.88 ± 0.02 which translates to a favourable Gibbs energy change of ΔG=–27.4 kJ/mol at 25 °C. This is in remarkable agreement with the computational docking G-scores for **CuL1** and **CuL2** which were –32.9 kJ/mol and –34.8 kJ/mol, respectively.

The ctDNA melting temperature obtained from Fig. 12 of 82 °C agrees with values observed in literature [63]. Typically, the binding of compounds to DNA results in an increase in the melting temperature. DNA intercalators for instance stabilise the double helix by their π-π stacking interactions which require more energy to break, thereby resulting in an increase in the melting temperature of DNA [64,65]. However, there are reported DNA binders that result in a decrease in the melting temperature observed. The binding of an intercalator may result in a small unwinding of the DNA helix to accommodate the compound and this may result in DNA elongation. The larger base pair distortion may result in diminished van der Waals forces which results in a decrease of the melting temperature of DNA [66]. Both complexes have a melting temperature that is > 5 °C lower than that of ctDNA alone which suggests that they destabilize the DNA helix upon binding.

4. Conclusion

We have presented solid-state X-ray data for two biomimetic models of the copper bilirubin complex. These dipyrromethene copper complexes bind DNA with a favourable Gibbs energy and a moderate-to-high affinity with log K_a ~ 5. The mechanism was found to be intercalative, and this model was simulated using molecular docking and dynamics. These findings suggest that the copper dipyrromethene complexes may affect therapeutic action through interaction with DNA. Further, our findings suggest that the copper-dipyrromethene moiety is a key feature for the therapeutic effects observed in copper complexes of bilirubin. Hence, further research is warranted involving *in vitro* cell cultures to

determine viability for drug development.

CCDC contains the supplementary crystallographic data for **CuL1** and **CuL2** (CCDC Deposition Numbers: **2,348,358** and **2348360**).

CRediT authorship contribution statement

Nabeelah Sarang: Writing – review & editing, Writing – original draft, Methodology, Investigation, Conceptualization. **Matthew L. Bracken:** Writing – review & editing, Writing – original draft, Methodology, Investigation, Formal analysis, Data curation. **Monika Nowakowska:** Supervision, Writing – review & editing. **Sadhna Mathura:** Writing – review & editing, Supervision, Funding acquisition, Conceptualization.

Declaration of competing interest

The authors declare that they have no known competing financial interests or personal relationships that could have appeared to influence the work reported in this paper.

Data availability

Data will be made available on request.

Acknowledgment

We thank the NRF and the University of the Witwatersrand for generous funding to enable the purchase of a dual wavelength hybrid diamond anode X-ray diffractometer (Bruker D8 Discovery Bio) under NEP Grant No 129920. We are also grateful for funding received under the NRF Grant MATH021. We also thank the Centre for High Performance Computing (Project CHEM1633, CHPC, Cape Town) for the access to the supercomputing infrastructure.

Appendix A. Supplementary data

Supplementary data to this article can be found online at https://doi.org/10.1016/j.poly.2024.117161.

References

[1] D.Y. Lee, J.Y. Kim, Y. Lee, S. Lee, W. Miao, H.S. Kim, J.-J. Min, S. Jon, Black pigment gallstone inspired platinum-chelated bilirubin nanoparticles for combined photoacoustic imaging and photothermal therapy of cancers, Angew. Chem. Int. Ed. Engl. 56 (2017) 13684–13688, https://doi.org/10.1002/anie.201707137.

[2] P. Fathi, H.J. Knox, D. Sar, I. Tripathi, F. Ostadhossein, S.K. Misra, M.B. Esch, J. Chan, D. Pan, Biodegradable biliverdin nanoparticles for efficient photoacoustic imaging, ACS Nano 13 (2019) 7690–7704, https://doi.org/10.1021/acsnano.9b01201.

[3] C. Lee, K. Lim, S.S. Kim, L.X. Thien, E.S. Lee, K.T. Oh, H.-G. Choi, Y.S. Youn, Near infrared light-responsive heat-emitting hemoglobin hydrogels for photothermal cancer therapy, Colloids Surf. B Biointerfaces 176 (2019) 156–166, https://doi.org/10.1016/j.colsurfb.2018.12.070.

[4] R. Xing, Q. Zou, C. Yuan, L. Zhao, R. Chang, X. Yan, Self-assembling endogenous biliverdin as a versatile near-infrared photothermal nanoagent for cancer theranostics, Adv. Mater. 31 (2019) e1900822.

[5] D.Y. Lee, S. Kang, Y. Lee, J.Y. Kim, D. Yoo, W. Jung, S. Lee, Y.Y. Jeong, K. Lee, S. Jon, PEGylated bilirubin-coated iron oxide nanoparticles as a biosensor for magnetic relaxation switching-based ROS detection in whole blood, Theranostics 10 (2020) 1997–2007, https://doi.org/10.7150/thno.39662.

[6] S.F. Asad, S. Singh, A. Ahmad, S.M. Hadi, Bilirubin-Cu(II) complex degrades DNA, Biochimica et Biophysica Acta (BBA) - General Subjects 1428 (1999) 201–208. https://doi.org/10.1016/S0304-4165(99)00075-6.

[7] S.F. Asad, S. Singh, A. Ahmad, S.M. Hadi, Bilirubin/biliverdin–Cu(II) induced DNA breakage; reaction mechanism and biological significance, Toxicol. Lett. 131 (2002) 181–189, https://doi.org/10.1016/S0378-4274(02)00031-0.

[8] S. Adhikari, P. Nath, A. Das, A. Datta, N. Baildya, A.K. Duttaroy, S. Pathak, A review on metal complexes and its anti-cancer activities: Recent updates from *in vivo* studies, Biomed. Pharmacother. 171 (2024) 116211, https://doi.org/10.1016/j.biopha.2024.116211.

[9] A proposed novel structure for the metal chelates of bilirubin. - PMC, (n.d.). https://www.ncbi.nlm.nih.gov/pmc/articles/PMC1174564/ (accessed June 29, 2024).

[10] Considerations concerning the fomration of metal chelates of bilirubin: the zinc-bilirubin system - PubMed, (n.d.). https://pubmed.ncbi.nlm.nih.gov/4433637/ (accessed June 29, 2024).

[11] J.D. Van Norman, M.M. Humans, Bilirubin–metal ion complexes, Anal. Chem. 46 (1974) 926–929, https://doi.org/10.1021/ac60343a033.

[12] R. Shikha Singh, R. Prasad Paitandi, R. Kumar Gupta, D. Shankar Pandey, Recent developments in metal dipyrrin complexes: design, synthesis, and applications, Coord. Chem. Rev. 414 (2020) 213269, https://doi.org/10.1016/j.ccr.2020.213269.

[13] N. Boens, B. Verbelen, M.J. Ortiz, L. Jiao, W. Dehaen, Synthesis of BODIPY dyes through postfunctionalization of the boron dipyrromethene core, Coord. Chem. Rev. 399 (2019) 213024, https://doi.org/10.1016/j.ccr.2019.213024.

[14] A. Bessette, G.S. Hanan, Design, synthesis and photophysical studies of dipyrromethene-based materials: insights into their applications in organic photovoltaic devices, Chem. Soc. Rev. 43 (2014) 3342–3405, https://doi.org/10.1039/C3CS60411J.

[15] S. Madhu, M.R. Rao, M.S. Shaikh, M. Ravikanth, 3,5-diformylboron dipyrromethenes as fluorescent pH sensors, Inorg. Chem. 50 (2011) 4392–4400, https://doi.org/10.1021/ic102499h.

[16] S.H. Lim, C. Thivierge, P. Nowak-Sliwinska, J. Han, H. van den Bergh, G. Wagnières, K. Burgess, H.B. Lee, In vitro and in vivo photocytotoxicity of boron dipyrromethene derivatives for photodynamic therapy, J. Med. Chem. 53 (2010) 2865–2874, https://doi.org/10.1021/jm901823u.

[17] R.K. Gupta, G. Sharma, R. Pandey, A. Kumar, B. Koch, P.-Z. Li, Q. Xu, D.S. Pandey, DNA/protein binding, molecular docking, and in vitro anticancer activity of some thioether-dipyrrinato complexes, Inorg. Chem. 52 (2013) 13984–13996, https://doi.org/10.1021/ic401662d.

[18] R.K. Gupta, R. Pandey, G. Sharma, R. Prasad, B. Koch, S. Srikrishna, P.-Z. Li, Q. Xu, D.S. Pandey, DNA binding and anti-cancer activity of redox-active heteroleptic piano-stool Ru(II), Rh(III), and Ir(III) complexes containing 4-(2-methoxypyridyl) phenyldipyrromethene, Inorg. Chem. 52 (2013) 3687–3698, https://doi.org/10.1021/ic302196v.

[19] E.A. Akanbong, M. Sudagidan, A.K. Devrim, DNA-metal interaction and the biological activities of metal complexes: an overview in the light of recent literature, (n.d.).

[20] N. Hadjiliadis, E. Sletten, Metal Complex-DNA Interactions (2009), https://doi.org/10.1002/9781444312089.

[21] C.J. Cardin, J.P. Hall, Structural studies of DNA-binding metal complexes of therapeutic importance, in: M.J. Waring (Ed.), DNA-Targeting Molecules as Therapeutic Agents, The Royal Society of Chemistry, 2018: pp. 198–227. https://doi.org/10.1039/9781788012928-00198.

[22] I. Iakovidis, I. Delimaris, S.M. Piperakis, Copper and its complexes in medicine: a biochemical approach, Molecular Biology International 2011 (2011) 1–13, https://doi.org/10.4061/2011/594529.

[23] C. Marzano, M. Pellei, F. Tisato, C. Santini, Copper complexes as anticancer agents, ACAMC 9 (2009) 185–211, https://doi.org/10.2174/187152009787313837.

[24] S. Tardito, L. Marchio, Copper compounds in anticancer strategies, CMC 16 (2009) 1325–1348, https://doi.org/10.2174/092986709787846532.

[25] P. Ji, P. Wang, H. Chen, Y. Xu, J. Ge, Z. Tian, Z. Yan, Potential of copper and copper compounds for anticancer applications, Pharmaceuticals 16 (2023) 234, https://doi.org/10.3390/ph16020234.

[26] D. Krishnan, A. Sheela, A review on DNA/BSA binding and cytotoxic properties of multinuclear Schiff's base complexes, Results in Chemistry 5 (2023) 100732, https://doi.org/10.1016/j.rechem.2022.100732.

[27] C. Molinaro, A. Martoriati, L. Pelinski, K. Cailliau, Copper complexes as anticancer agents targeting topoisomerases I and II, Cancers 12 (2020) 2863, https://doi.org/10.3390/cancers12102863.

[28] M.R. Rodríguez, M.J. Lavecchia, B.S. Parajón-Costa, A.C. González-Baró, M. R. González-Baró, E.R. Cattáneo, DNA cleavage mechanism by metal complexes of Cu(II), Zn(II) and VO(IV) with a schiff-base ligand, Biochimie 186 (2021) 43–50, https://doi.org/10.1016/j.biochi.2021.04.002.

[29] T. Vitomirov, F. Dimiza, I.Z. Matić, T. Stanojković, A. Pirković, L. Živković, B. Spremo-Potparević, I. Novaković, K. Anđelković, M. Milčić, G. Psomas, M.Š. Ristović, Copper(II) complexes with 4-(diethylamino)salicylaldehyde and α-diimines: anticancer, antioxidant, antigenotoxic effects and interaction with DNA and albumins, J. Inorg. Biochem. 235 (2022) 111942, https://doi.org/10.1016/j.jinorgbio.2022.111942.

[30] K.D. Mjos, C. Orvig, Metallodrugs in medicinal inorganic chemistry, Chem. Rev. 114 (2014) 4540–4563, https://doi.org/10.1021/cr400460s.

[31] F. Tisato, C. Marzano, M. Porchia, M. Pellei, C. Santini, Copper in diseases and treatments, and copper-based anticancer strategies, Med. Res. Rev. 30 (2010) 708–749, https://doi.org/10.1002/med.20174.

[32] A. Kellett, Z. Molphy, V. McKee, C. Slator, Recent advances in anticancer copper compounds, in: A. Casini, A. Vessières, S.M. Meier-Menches (Eds.), Metal-Based Anticancer Agents, The Royal Society of Chemistry, 2019: pp. 91–119. https://doi.org/10.1039/9781788016452-00091.

[33] R. Galindo-Murillo, J.C. Garcia-Ramos, L. Ruiz-Azuara, T.E. Cheatham, F. Cortes-Guzman, Intercalation processes of copper complexes in DNA, Nucleic Acids Res. 43 (2015) 5364–5376, https://doi.org/10.1093/nar/gkv467.

[34] L. Qian, T. Miao, L. Xu, Probing DNA-cleavage efficiencies of copper(II) complexes: a computational perspective, ACS Omega 5 (2020) 19029–19033, https://doi.org/10.1021/acsomega.0c02331.

[35] Bruker, APEX4version 2021.4-1 data collection software which includes SAINT version 8.40B, SADABS-2016/2, and XPREP version 2014/2. Bruker AXS Inc., Madison, Wisconsin, USA., (2021) (n.d.).

[36] O.V. Dolomanov, L.J. Bourhis, R.J. Gildea, J.A.K. Howard, H. Puschmann,. J. Appl. Cryst. 42, (2009) 339-341., (n.d.).
[37] G.M. Sheldrick, Acta Cryst. A71, (2015) 3-8., (n.d.).
[38] G.M. Sheldrick, Acta Cryst., 2015, C71, 3-8., (n.d.).
[39] A.J.F.N. Sobral, N.G.C.L. Rebanda, M. da Silva, S.H. Lampreia, M. Ramos Silva, A. M. Beja, J.A. Paixão, A.M. d'A Rocha Gonsalves, One-step synthesis of dipyrromethanes in water, Tetrahedron Lett. 44 (2003) 3971–3973, https://doi.org/10.1016/S0040-4039(03)00785-8.
[40] T. Rohand, E. Dolusic, T.H. Ngo, W. Maes, W. Dehaen, Efficient synthesis of aryldipyrromethanes in water and their application in the synthesis of corroles and dipyrromethenes, ARKIVOC 2007 (2007) 307–324, https://doi.org/10.3998/ark.5550190.0008.a20.
[41] C. Brückner, V. Karunaratne, S.J. Rettig, D. Dolphin, Synthesis of meso -phenyl-4,6-dipyrrins, preparation of their Cu(II), Ni(II), and Zn(II) chelates, and structural characterization of bis[meso -phenyl-4,6-dipyrrinato]Ni(II), Can. J. Chem. 74 (1996) 2182–2193, https://doi.org/10.1139/v96-245.
[42] M.J. Frisch, G.W. Trucks, H.B. Schlegel, G.E. Scuseria, M.A. Robb, J.R. Cheeseman, G. Scalmani, V. Barone, G.A. Petersson, H. Nakatsuji, X. Li, M. Caricato, A.V. Marenich, J. Bloino, B.G. Janesko, R. Gomperts, B. Mennucci, H.P. Hratchian, J.V. Ortiz, A.F. Izmaylov, J.L. Sonnenberg, D. Williams-Young, F. Ding, F. Lipparini, F. Egidi, J. Goings, B. Peng, A. Petrone, T. Henderson, D. Ranasinghe, V.G. Zakrzewski, J. Gao, N. Rega, G. Zheng, W. Liang, M. Hada, M. Ehara, K. Toyota, R. Fukuda, J. Hasegawa, M. Ishida, T. Nakajima, Y. Honda, O. Kitao, H. Nakai, T. Vreven, K. Throssell, J.A. Montgomery, Jr., J.E. Peralta, F. Ogliaro, M.J. Bearpark, J. J. Heyd, E.N. Brothers, K.N. Kudin, V.N. Staroverov, T.A. Keith, R. Kobayashi, J. Normand, K. Raghavachari, A.P. Rendell, J.C. Burant, S.S. Iyengar, J. Tomasi, M. Cossi, J.M. Millam, M. Klene, C. Adamo, R. Cammi, J.W. Ochterski, R.L. Martin, K. Morokuma, O. Farkas, J.B. Foresman, D.J. Fox, Gaussian 16, Revision C.01, (2016).
[43] T. Yanai, D.P. Tew, N.C. Handy, A new hybrid exchange–correlation functional using the Coulomb-attenuating method (CAM-B3LYP), Chem. Phys. Lett. 393 (2004) 51–57, https://doi.org/10.1016/j.cplett.2004.06.011.
[44] C.E. Check, T.O. Faust, J.M. Bailey, B.J. Wright, T.M. Gilbert, L.S. Sunderlin, Addition of polarization and diffuse functions to the LANL2DZ basis set for P-block elements, Chem. A Eur. J. 105 (2001) 8111–8116, https://doi.org/10.1021/jp011945l.
[45] R. Dennington, T.A. Keith, J.M. Millam, GaussView Version 6 (2019).
[46] F. Lipparini, G. Scalmani, B. Mennucci, E. Cancès, M. Caricato, M.J. Frisch, A variational formulation of the polarizable continuum model, J. Chem. Phys. 133 (2010) 014106, https://doi.org/10.1063/1.3454683.
[47] H. Rozenberg, D. Rabinovich, F. Frolow, R.S. Hegde, Z. Shakked, Structural code for DNA recognition revealed in crystal structures of papillomavirus E2-DNA targets, PNAS 95 (1998) 15194–15199, https://doi.org/10.1073/pnas.95.26.15194.
[48] H. Song, J.T. Kaiser, J.K. Barton, Crystal structure of Δ-[Ru(bpy)2d ppz]2+ bound to mismatched DNA reveals side-by-side metalloinsertion and intercalation, Nature Chem 4 (2012) 615–620, https://doi.org/10.1038/nchem.1375.
[49] G. Madhavi Sastry, M. Adzhigirey, T. Day, R. Annabhimoju, W. Sherman, Protein and ligand preparation: parameters, protocols, and influence on virtual screening enrichments, J. Comput. Aided Mol. Des. 27 (2013) 221–234, https://doi.org/10.1007/s10822-013-9644-8.
[50] J.C. Shelley, A. Cholleti, L.L. Frye, J.R. Greenwood, M.R. Timlin, M. Uchimaya, Epik: a software program for pK a prediction and protonation state generation for drug-like molecules, J. Comput. Aided Mol. Des. 21 (2007) 681–691, https://doi.org/10.1007/s10822-007-9133-z.
[51] J.L. Banks, H.S. Beard, Y. Cao, A.E. Cho, W. Damm, R. Farid, A.K. Felts, T. A. Halgren, D.T. Mainz, J.R. Maple, R. Murphy, D.M. Philipp, M.P. Repasky, L. Y. Zhang, B.J. Berne, R.A. Friesner, E. Gallicchio, R.M. Levy, Integrated modeling program, applied chemical theory (IMPACT), J. Comput. Chem. 26 (2005) 1752–1780, https://doi.org/10.1002/jcc.20292.
[52] R.A. Friesner, J.L. Banks, R.B. Murphy, T.A. Halgren, J.J. Klicic, D.T. Mainz, M. P. Repasky, E.H. Knoll, M. Shelley, J.K. Perry, D.E. Shaw, P. Francis, P.S. Shenkin, Glide: a new approach for rapid, accurate docking and scoring. 1. method and assessment of docking accuracy, J. Med. Chem. 47 (2004) 1739–1749, https://doi.org/10.1021/jm0306430.
[53] R.A. Friesner, R.B. Murphy, M.P. Repasky, L.L. Frye, J.R. Greenwood, T.A. Halgren, P.C. Sanschagrin, D.T. Mainz, Extra precision glide: docking and scoring incorporating a model of hydrophobic enclosure for protein−ligand complexes, J. Med. Chem. 49 (2006) 6177–6196, https://doi.org/10.1021/jm051256o.
[54] K.J. Bowers, D.E. Chow, H. Xu, R.O. Dror, M.P. Eastwood, B.A. Gregersen, J. L. Klepeis, I. Kolossvary, M.A. Moraes, F.D. Sacerdoti, J.K. Salmon, Y. Shan, D. E. Shaw, Scalable Algorithms for Molecular Dynamics Simulations on Commodity Clusters, in: ACM/IEEE SC 2006 Conference (SC'06), IEEE, Tampa, FL, 2006, p. 43, https://doi.org/10.1109/SC.2006.54.
[55] W.L. Jorgensen, J. Chandrasekhar, J.D. Madura, R.W. Impey, M.L. Klein, Comparison of simple potential functions for simulating liquid water, J. Chem. Phys. 79 (1983) 926–935, https://doi.org/10.1063/1.445869.
[56] W.L. Jorgensen, Convergence of Monte Carlo simulations of liquid water in the NPT ensemble, Chem. Phys. Lett. 92 (1982) 405–410, https://doi.org/10.1016/0009-2614(82)83437-4.
[57] P.C. Dedon, Determination of binding mode: intercalation, Curr Protoc Nucleic Acid Chem Chapter 8 (2001) Unit 8.1. https://doi.org/10.1002/0471142700.nc0801s00.
[58] H. Luo, Y. Liang, H. Zhang, Y. Liu, Q. Xiao, S. Huang, Comparison on binding interactions of quercetin and its metal complexes with calf thymus DNA by spectroscopic techniques and viscosity measurement, J. Mol. Recognit. 34 (2021) e2933.
[59] M.S. Ragab, M.R. Shehata, M.M. Shoukry, M. Haukka, M.A. Ragheb, Oxidative DNA cleavage mediated by a new unexpected [Pd(BAPP)][PdCl 4] complex (BAPP = 1,4-bis(3-aminopropyl)piperazine): crystal structure, DNA binding and cytotoxic behavior, RSC Adv. 12 (2022) 1871–1884, https://doi.org/10.1039/D1RA07793G.
[60] M.S. Surendra Babu, B.U. Rao, V. Krishna, S. Mustafa, G.N. Rao, Synthesis, characterization and DNA cleavage studies of isomeric pyridyl-tetrazole ligands and their Ni(II) and Zn(II) complexes, J. Saudi Chem. Soc. 21 (2017) 291–299, https://doi.org/10.1016/j.jscs.2015.07.003.
[61] N. Kumar, R. Kaushal, P. Awasthi, Non-covalent binding studies of transition metal complexes with DNA: a review, J. Mol. Struct. 1288 (2023) 135751, https://doi.org/10.1016/j.molstruc.2023.135751.
[62] R. Gesztelyi, J. Zsuga, A. Kemeny-Beke, B. Varga, B. Juhasz, A. Tosaki, The Hill equation and the origin of quantitative pharmacology, Arch. Hist. Exact Sci. 66 (2012) 427–438, https://doi.org/10.1007/s00407-012-0098-5.
[63] V. Visone, I. Szabó, G. Perugino, F. Hudecz, Z. Bánóczi, A. Valenti, Topoisomerases inhibition and DNA binding mode of daunomycin–oligoarginine conjugate, J. Enzyme Inhib. Med. Chem. 35 (2020) 1363–1371, https://doi.org/10.1080/14756366.2020.1780226.
[64] W.D. Wilson, F.A. Tanious, M. Fernandez-Saiz, C.T. Rigl, Evaluation of drug–nucleic acid interactions by thermal melting curves, in: Drug-DNA Interaction Protocols, Humana Press, New Jersey, 1997: pp. 219–240. https://doi.org/10.1385/0-89603-447-X:219.
[65] J.A. Bueren-Calabuig, C. Giraudon, C.M. Galmarini, J.M. Egly, F. Gago, Temperature-induced melting of double-stranded DNA in the absence and presence of covalently bonded antitumour drugs: insight from molecular dynamics simulations, Nucleic Acids Res. 39 (2011) 8248–8257, https://doi.org/10.1093/nar/gkr512.
[66] G. Lenglet, M.-H. David-Cordonnier, DNA-destabilizing agents as an alternative approach for targeting DNA: mechanisms of action and cellular consequences, J. Nucleic Acids 2010 (2010) 290935, https://doi.org/10.4061/2010/290935.